JGR Solid Earth

RESEARCH ARTICLE
10.1029/2020JB020270

Key Points:
- We investigate the efficiency of *P*-wave coda autocorrelation in recovering crustal architecture
- We compare imaging from *P*-wave coda vertical autocorrelations and radial receiver functions using dense profiles from US arrays
- Vertical autocorrelations clearly outperform radial receiver functions in presence of a sedimentary basin

Supporting Information:
- Supporting Information S1

Correspondence to:
B. Tauzin,
benoit.tauzin@univ-lyon1.fr

Citation:
Wang, C., Tauzin, B., Pham, T.-S., & Tkalčić, H. (2020). On the efficiency of *P*-wave coda autocorrelation in recovering crustal structure: Examples from dense arrays in the eastern United States. *Journal of Geophysical Research: Solid Earth*, *125*, e2020JB020270. https://doi.org/10.1029/2020JB020270

Received 26 MAY 2020
Accepted 6 NOV 2020
Accepted article online 12 NOV 2020

On The Efficiency of *P*-Wave Coda Autocorrelation in Recovering Crustal Structure: Examples From Dense Arrays in the Eastern United States

Chuang Wang[1,2], Benoît Tauzin[1,3], Thanh-Son Pham[1], and Hrvoje Tkalčić[1]

[1]Research School of Earth Sciences, The Australian National University, Canberra, ACT, Australia, [2]Now at Earth Sciences and CODES, University of Tasmania, Hobart, Australia, [3]Université de Lyon, Université Claude Bernard Lyon 1, ENS, CNRS, Laboratoire de Géologie de Lyon: Terre, Planètes, Environnement, Lyon, France

Abstract Due to a sharp contrast in elastic properties across the basement rocks of sedimentary basins (SBs), strong reverberations are generated during the passage of seismic waves. Traditional receiver function methods become inadequate for imaging crustal structure due to the existence of these strong reverberations. We investigate the feasibility of an autocorrelation technique to extract vertical component receiver functions from teleseismic earthquake data and the efficiency of the method to image the crustal architecture in presence of a SB. The method involves spectral whitening followed by autocorrelation and stacking in the depth domain. We show promising results when using temporary seismic networks in the eastern United States. Using synthetic and field-data examples, we demonstrate that vertical autocorrelations are more efficient than classical radial receiver functions for interpretation purposes in an SB context. We also perform a joint analysis of the amplitudes on radial and vertical receiver functions for characterizing the thickness of the Mohorovičić discontinuity (Moho). We find that the Moho in the eastern United States is a transitional layer (up to 5-km thick) instead of a sharp boundary. Further, we point out that it is challenging to unambiguously pick and interpret reflected phases on autocorrelations because of the effects of reverberations, cross-mode contaminations, and a narrow frequency band limiting the resolution of velocity gradients. We therefore send a message of caution for future interpretations based on this technique.

1. Introduction

Teleseismic earthquakes occur at distances of more than thousands of kilometers away from the recorders (typically epicentral distances larger than 30°). At these epicentral distances, the incoming teleseismic wave is approximately a plane wave with a relatively steep incidence angle. Burdick and Helmberger (1974) noticed that vertically polarized teleseismic waveforms are dominated by the source, the near-source structure, and the instrument effects. The near-receiver structure, due to a small incidence angle, influences mainly the compressional wave (*P* wave) response in the vertical seismograms. Similarly, the shear wave (*S* wave) response of the structure beneath a receiver can be retrieved from the horizontal seismograms. Langston (1979) proposed a technique to determine the near-receiver structural response by deconvolving the vertical component of teleseismic seismograms from the horizontal ones. Through deconvolution, the complicated source and wavefield propagation effects away from the receiver are removed from the horizontal components, and the results are referred to as the radial receiver functions (RFs). Vinnik (1977) introduced slightly earlier the correlation-based approach to compute receiver functions.

The introduction of auto- and cross-correlations to seismology predated the development of the RF method. The autocorrelation of the transmission response of an acoustic plane-wave was used by Claerbout (1968) to extract the reflection response of the stratification beneath a receiver. Autocorrelation is a mathematical operation that measures the similarity of a waveform with itself in a single time series. A similar operation, cross-correlation, involves two seismograms, and is used to build the radial RF with deconvolution (Ammon, 1991; Clayton & Wiggins, 1976; Vinnik, 1977). In the following, we will interchangeably use the terminology "autocorrelation" and "vertical RF" because in practice the vertical RF can be built from the autocorrelation of the vertical component seismogram (Tauzin et al., 2019).

A few early studies used the principle of correlation for characterizing crustal structure (e.g., Burdick & Langston, 1977; Langston & Hammer, 2001; Li & Nábělek, 1999). In particular, Langston and Hammer (2001) suggested that all three components of the RFs should be involved in inferring Earth-structure models and demonstrated the reliability of the technique by means of using vertical-component *P*-wave (autocorrelation) RFs. More recent developments of the autocorrelation method make use of the vertically propagating component of the seismic ambient noise (e.g., Becker & Knapmeyer-Endrun, 2018; Gorbatov et al., 2013; Kennett, 2015; Kennett, Saygin & Salmon 2015; Saygin et al., 2017; Taylor et al., 2016; Tibuleac & von Seggern, 2012). The difference between the noise-based and event-based approaches is still under investigation (Buffoni et al., 2019; Kennett, 2015; Romero & Schimmel, 2018; Sun & Kennett, 2016; Tauzin et al., 2019). The choice of filtering have been shown to play an important role in the recovery and type of recovered signal from noise autocorrelations (Helffrich, 2019) with two main approaches. The first approach is inherited from standard radial RFs analysis and makes use of frequencies smaller than 1 Hz (Taylor et al., 2016; Tibuleac & von Seggern, 2012). This approach allows for the identification of individual reflected phases on autocorrelograms for subsequent picking and interpretation in terms of stratigraphy. The second approach makes use of the high-frequency component of the noise that involves an analysis within a narrow frequency band (Becker & Knapmeyer-Endrun, 2018; Gorbatov et al., 2013; Kennett, 2015; Romero & Schimmel, 2018). In this second case, deterministic seismic arrivals are not anymore detected, and the interpretation is driven by changes in the reflectivity patterns in autocorrelations.

In sedimentary basins (SBs), radial RFs are contaminated by a strong resonance effect. As shown by, for example, Zheng et al. (2005), RFs from recording sites that are filled by sediments are dominated by reverberations in the sedimentary layers within the first few seconds after the direct *P* arrival. Indeed, due to a strong, basal, impedance contrast, the low-velocity sedimentary layer (LVZ) generates quite strong *P*-wave and *S*-wave reverberations and conversions. The superimposed reflections and conversion at the base the sediments often dominate over the converted phases from deeper crustal discontinuities and mask corresponding information about Earth structure (Frederiksen & Delaney, 2015). Thus, conventional methods based on the analyses of travel times of converted waves can lead to erroneous interpretations.

Several methods have been developed for mapping the crustal structure in SBs. Those methods, designed to reduce SB reverberations, include downward continuation and wavefield decomposition (Langston, 2011), autocorrelation with a resonance removal filter in the frequency domain (Yu et al., 2015), and radial RF method to fit the waveforms and invert for elastic structure of a SB (Piana Agostinetti et al., 2018). Wavefield downward continuation method (Langston, 2011) requires a priori knowledge of Earth structure and modeling to extract wave conversions. This method has been applied to estimate sedimentary and crustal structures (e.g., Tao et al., 2014). Another recent study investigated sedimentary structure of basins in China from frequency dependent *P*-wave particle motion (Yang & Niu, 2019). Li et al. (2019) reported a joint inversion of Rayleigh wave phase velocity, particle motion, and teleseismic body wave data for sedimentary structures.

Here, we investigate the performance of a new method for imaging the crustal architecture based on the spectral whitening and autocorrelation of the vertical component of teleseismic records (Pham & Tkalčić, 2017; Tauzin et al., 2019). We investigate whether this method is appropriate for characterizing the crustal structure in the presence of a SB. Spectral whitening is the division in the frequency domain of the original spectrum by the running average of its amplitude. We show that this operation efficiently filters out undesirable resonance associated with SBs. In comparison to the inversion of radial RF waveforms, autocorrelation based on filtering is computationally efficient for achieving direct imaging of the basin and crustal structure.

In order to demonstrate our method with dense seismic arrays, we analyze broadband data from temporary seismic arrays with quasi-linear geometry in the eastern United States. Recently, two studies have used the principle of correlation to analyze the crustal structure in the United States. Delph et al. (2019) constrained the Moho depth and crustal v_p/v_s ratio underneath 88 stations from the transportable array using vertical and radial component RFs. van IJsseldijk et al. (2019) used a dense seismic array in Minnesota and Wisconsin and a global-phase seismic interferometry approach, which is based on autocorrelations of teleseismic *P* waveforms, but recorded at small incidence angles.

The seismic arrays that we use for imaging the crust in eastern United States run from the Quaternary deposits in the Mississippi embayment, through a region of thickened crust at the western border of the Appalachian, to Maine in the northeast. Our data are divided into three subarrays with various station densities and operation times that sample different geological settings. We investigate in particular the efficiency

10.1029/2020JB020270

of the method for imaging a laterally variable crust overlaid in places by SBs. We present the general features of the processing. Given the amount of data and the processing for source equalization, a data selection procedure is implemented, which is dedicated to improving the signal-to-noise ratio of specific reflected arrivals. We observed coherent signals along the three subarrays. A comparison with a reference crustal model suggests that we unambiguously image the Moho and the internal stratification of the crust, in contrary to radial RFs that poorly perform in presence of a SB. We also find in the eastern United States the Moho to be a transitional layer (up to 5-km thick) instead of a sharp boundary.

2. Methods and Data

An example of vertical component RF for a simple one-layer crust is shown in Figure 1b, with labels for major converted and reflected phases *Ps*, *PPp*, *PPs*, and *PSs*. The paths are shown in Figure 1a. We also show in Figure 1b for comparison the theoretical response recorded on the radial component. In our particular implementation of the vertical receiver function method, the extracted signal corresponds to the sequence of reflections (Figure 1b) in the stratification underneath the seismometer (Figure 1a). The main reflection being recorded on this vertical RF is the reflection from the top of the Moho discontinuity, PPmp, where “m” marks the Moho (Figure 1b). Its amplitude results from the interaction of the teleseismic wavefield with the free surface, with a reflection coefficient close to −1, and with the Moho interface, with a positive reflection coefficient. The combined reflection response gives a negative amplitude for the Moho reflection on the vertical RF record (Figure 1b). This response is not exactly the reflection response as obtained within the frame of seismic interferometry (Claerbout, 1968; Ruigrok & Wapenaar, 2012; Tauzin et al., 2019; Wapenaar et al., 2010). Indeed, if we take the reflection response due to a virtual source located at the surface at the reflection point of the teleseismic *P* wave, then the negative reflection at the free surface is removed through the principle of interferometry, and the remaining reflection at the Moho is positive. Our estimated reflection response has therefore an opposite (negative) sign with respect to the *P*-wave reflection response in seismic interferometry imaging applications.

We compute the vertical RFs using spectral whitening, followed by autocorrelation (Pham & Tkalčić, 2017; Tauzin et al., 2019). If $Z(f)$ is the spectrum of the vertical component, the vertical receiver function $E_z(f)$ is obtained from

$$E_z(f) \approx \frac{Z(f)Z^*(f)}{Z''(f)}, \tag{1}$$

where the superscript * marks the complex conjugate and $Z(f)Z^*(f)$ is the autocorrelation written in the frequency domain. $Z''(f)$ is the regularized vertical component power spectrum taken as an approximation for the teleseismic source function. Each frequency sample is obtained through smoothing over a window of width W so the regularized vertical spectrum is

$$Z''(f) = \frac{1}{W}\int_{f-W/2}^{f+W/2} ||Z(\nu)||^2 d\nu. \tag{2}$$

In the postprocessing stage, we apply a fourth-order Butterworth filter with a band pass chosen depending on the target structure. The frequency content necessary to image the shallow structure is higher (0.4- to 1-Hz band pass) than for imaging the Moho (0.2- to 1-Hz band pass). We also use different values of the smoothing width W depending on the target interface (see Pham & Tkalčić, 2018). We discuss the choice of the W parameter in section 5.3. We use a constant value of $W = 0.1$ Hz for targeting the Moho. We set W to a larger value, 0.4 Hz, when targeting the shallow stratification.

To improve the signal-to-noise ratio, all the vertical component RFs for a single station are stacked to build a high-quality reflection response. As the RFs are obtained over a large range of epicentral distances, the travel time of *P*-wave reflected phases follows a move-out due to the variable path-lengths of waves incoming on the stratification (see examples in Figures S4-S7). For a single layer of thickness H and *P*-wave velocity v_p overlying a homogeneous half space, the travel time of the *PPp* mode with respect to direct *P* (Figure 1b) is expressed by

$$T_{PPp}(H, v_p, p) = 2H\sqrt{\frac{1}{v_p^2} - p^2}, \tag{3}$$

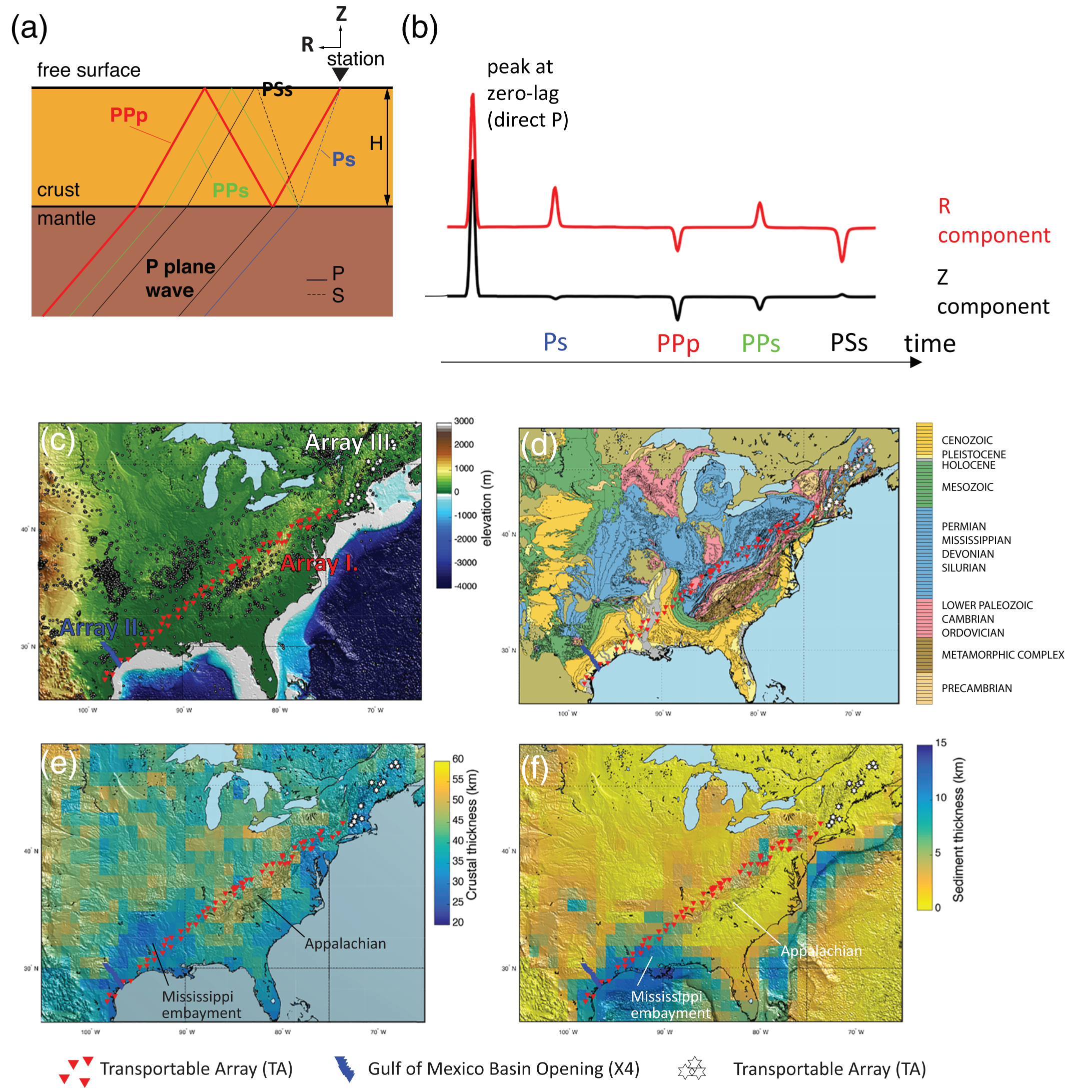

Figure 1. (a) *P*-wave reverberations from teleseismic records. The seismic stations (black inverted triangle) sits on top of the crust (orange) above the mantle (brown). The thickness of the crust is denoted as *H*. *P* wave is marked by solid lines and *S* wave by dashed lines. The phases most relevant in this study are shown as *Ps* (blue), *PPp* (red), *PPs* (green), and *PSs* (black). (b) Vertical (black) and radial (red) responses of the ground below the receiver for a simple, one-layer crust. In the vertical RF, the PPmp (*PPp*) and PPms (*PPs*) phases both exists, but PPmp is much stronger (Tauzin et al., 2019). (c) Topography, together with seismic subarrays used in this study and the seismicity (black circles) from the USGS catalog. (d) Main geological deposits color-coded as a function of age (Schruben et al., 1998). (e) Seismic subarrays and crustal thickness taken from the globally compiled model CRUST1.0 (Laske et al., 2013). (f) Sedimentary cover taken from CRUST1.0. The arrays belong to the following networks: Subarray I (red triangles) TA, transportable array; Subarray II (blue triangles) X4, Gulf of Mexico Basin Opening; Subarray III (white hexagrams) TA, transportable array.

where p is the slowness of the impinging P wave. We use the generalization of this expression to horizontally stratified media to compute a time-to-depth relationship and convert the time-domain autocorrelations into the depth domain (Tauzin et al., 2019). This relationship is mode dependent and leads after stacking to destructive interference of signals that do not follow the move-out of *P*-wave reflections *PPp*. Single-station autocorrelations are linearly stacked in the depth domain. Due to the fact that the PPms phase has a similar travel-time relation as PPmp, the PPms phase appears as a deeper "second Moho" with weaker amplitude (see Z component in Figure 1b). We tested phase-weighted stacking (Schimmel & Paulssen, 1997) but did not find a major improvement in the quality of crustal images. We apply bootstrap resampling (Efron & Tibshirani, 1991) for estimating the variability of stacked waveforms.

Despite the fact that Equation 1 can be modified to extract radial receiver functions (Tauzin et al., 2019), we computed classical radial receiver functions through water-level deconvolution (Clayton & Wiggins, 1976). The difference resides in the (quasi-)absence of the *PPp* mode in water-level receiver functions (Tauzin et al., 2019). In that case, the radial RF is given by

$$E_r(f) \approx \frac{R(f)Z^*(f)}{Z'(f)}, \tag{4}$$

where $R(f)$ is the radial component spectrum. The regularized vertical spectrum $Z'(f)$ is the initial spectrum that is leveled to a minimum amplitude defined by the water-level c (Clayton & Wiggins, 1976),

$$Z'(f) = max(||Z(f)||^2, c||Z||^2_{max}). \tag{5}$$

We apply in this case a Gaussian filter (Ammon, 1991; Clayton & Wiggins, 1976). The radial RFs are then depth-converted using a time-to-depth relationship for the direct *Ps* conversion mode

$$T_{Ps}(H, v_p, v_s, p) = H\left[\sqrt{\frac{1}{v_s^2} - p^2} - \sqrt{\frac{1}{v_p^2} - p^2}\right]. \tag{6}$$

Radial RFs at a single station in the depth domain are then linearly stacked to build the conversion response.

These methods are applied to broadband stations located in the eastern United States (Figure 1). This choice is motivated by the presence of seismic arrays with various station densities and operation times that sample different geological settings. We investigate in particular the efficiency of the method for imaging a laterally variable crust underlying in places thick SBs such as in the Mississippi Embayment. Our data are separated in three subarrays (Figure 1). We use the global crustal model Crust1.0 (Laske et al., 2013) and the geology of the conterminous United States (King & Beikman, 1974; Schruben et al., 1994) to describe the a priori structure beneath these arrays (Figure 1). We benefit from the transportable array for constructing transects of the crustal structure over several thousand kilometers with an average interstation spacing of 70 km (Subarrays I and III). We distinguish Subarray I from III because they sample different geological structures. Subarray I samples the thick sedimentary cover (up to 11 km) and thin crust (25–30 km) in the Mississippi embayment at southwest and the western border of the Appalachian in the middle with a thicker crust (up to 50 km) and thinner sedimentary cover (3-km thick) whereas Subarray III in Maine samples a standard crust (30-km thick) with no sedimentary cover. Finally, the Gulf of Mexico Basin Opening experiment (Array II) is a linear array with 15-km interstation spacing sampling sharp lateral changes of crustal and sedimentary thickness. Over 250 km, the model Crust1.0 indicates that the crust thins from 50 km at northwest to 35 km at the southeast, and the sedimentary cover increases in thickness from 0 to 11 km. The 15-km interstation spacing of Subarray II allows testing another imaging principle, common reflection point (CRP) migration (Tauzin et al., 2019), which unfolds the information on the structure by projecting amplitude on the RFs onto the final leg of the path of reflected waves underneath the receivers (supporting information, Figure S11).

The set of data used in this study is the same as used for classical radial RF studies. Metadata and data are provided by the Incorporated Research Institutions for Seismology (IRIS) data center (DMC) (Ahern et al., 2007) and the Global Centroid Moment Tensor (GCMT) catalog (Ekström et al., 2012). We used three-component stations with the broadband channel BH, and selected events from the GCMT catalog with moment magnitudes larger than 5.5 and epicentral distances between 30° and 90° to avoid the effect of triplications at mantle transition zone discontinuities and the core shadow zone. The processing is implemented using Matlab® scientific programming language, with the routine available online (http://perso.ens-lyon.fr/benoit.tauzin/data.htm).

The seismograms were extracted and preprocessed to remove asynchronous records on the three components, resampled, and projected to the desired vertical-radial-transverse component orientations. We selected data with seismogram signal-to-noise ratio larger than 1.7, the signal and noise being measured from a root mean square over windows following ([0 3.25] s) and preceding ([−2.5 −0.5] s) the theoretical *P*-wave arrival (at 0 s) in the *iasp91* model (Kennett & Engdahl, 1991). The seismograms are preprocessed to start 20 s before the *P*-wave arrival with a duration of 80 s. The seismograms are then processed using Equations 1 and 4, that is, applying spectral whitening and autocorrelation to build vertical RFs and water-level deconvolution for radial RFs.

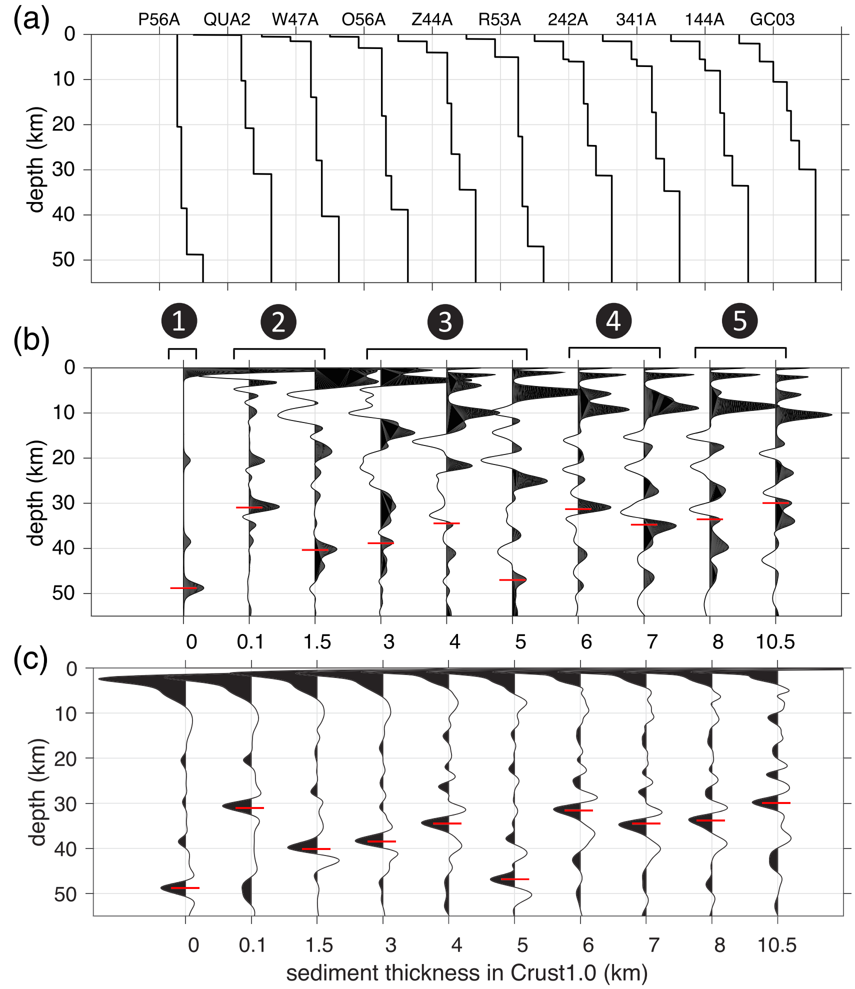

Figure 2. Reference *P*-wave velocity profiles (a) and corresponding synthetic radial (b) and vertical receiver functions (c) for 10 selected stations with increasing thickness of the sedimentary cover according to Crust1.0. The red lines indicate the Moho depth in Crust1.0. The vertical RFs are processed with $W = 0.1$ Hz.

The time-to-depth relationships, that is, Equations 3 and 6, are computed based on the velocity structure in the Crust1.0 model (Laske et al., 2013) at corresponding station locations. Crust1.0 is not taken here as providing the ground truth, but serves for a comparison with the observed data as well as guiding the interpretation of the recovered reflectivity. Crust1.0 is a global model that provides crustal types, thickness, and elastic properties of the crystalline crust according to basement age and tectonic setting (Laske et al., 2013). The Moho depth in particular is constrained by data from active-source seismic studies as well as radial RF analysis. So this model provides a good reference for calibrating our seismic images and discussing the deviation of the first-order structure from this model. The model in each cell is described as an eight-layer profile, including three sedimentary layers and three crustal layers. The parameters including *P*- and *S*-wave velocity, v_p, v_s, density, ρ, and thickness, H, are given for each layer. Crust1.0 is discretized over a $1 \times 1°$ pixel spatial grid (Laske et al., 2013). We do not expect to recover exactly the same structure beneath stations that do not have contributed to the model. This is the case for Array II, which is densely sampling the equivalent of ~2.5 cells of the Crust1.0 model (Figure 1). In all our applications, we compare the result of processing the observed data to synthetic data computed based on this global crustal model. We simulate the waveforms with the plane-wave matrix algorithm, "respknt" (Kennett, 1983; Randall, 1989). Synthetics waveforms are computed for the same acquisition geometry as in the observed data and processed with the same strategy: filtering, autocorrelation/deconvolution, time-to-depth conversion, and stacking. This approach is applied in all our synthetic experiments (Figures 2, 6, 7, 9e, 10, 11, and S4–S7), except Figures 9a–9d where the slowness is 0.06 s/km.

For observed data, we found in a preliminary attempt that the selection based on a signal-to-noise criterion applied on seismograms alone is not sufficient to ensure good quality autocorrelation stacks. At frequencies investigated here, the noise on single autocorrelations is a combination of incoherent (ambient) noise and signal-generated noise. The signal-generated noise is a result of the teleseismic source function: it includes the characteristics of the seismic source (slip history, radiation pattern, and source spectrum) as well as the effects of wave propagation near the source. In addition, interfering phases, such as PP or PcP, add complexity unrelated to the receiver-side structure. Stacking a large number of data is required to decrease the noise level to the acceptable level (Tauzin et al., 2019). But because we use temporary arrays (Figure 1), the number of available data is relatively small, which limits the performance of the stacking operation. Our experiments showed that at stations with a small number of data, even an application of a stacking with weighting based on the instantaneous phase (Schimmel & Paulssen, 1997) is not able to provide satisfying results. We therefore discarded all stations with less than 10 (for Subarrays I and III) or 15 (Subarray II) available autocorrelations.

We also relied on a more discriminative approach for data selection based on the use of a "phasing depth diagram." We use trial depths of seismic interfaces (phasing depths) and select traces that constructively contribute to the stacked signal at this depth. We provide in Figure S1 an illustrative diagram of the procedure, and in Figures S2 and S3 two examples based on simple synthetic signals and field data, respectively. For a negative signal corresponding to an interface at X-km depth, we first make a selection of the traces with a negative signal within ± 5 km from X-km depth. We then stack the selected traces with bootstrap resampling. Because the traces are depth-converted, a successful selection of traces contributing to build a signal at X-km depth should contribute to align (and build after stacking) signals for discontinuities at other depths. We retain only the traces that contribute to these multiple depths. We show in the supporting information how we use such a diagram juxtaposing stacked depth domain traces as a function of trial depths (the phasing depth diagram) to select a distribution of good quality data for a given station (Figures S1 and S3). This selective stacking method is more efficient applied to vertical RFs than to regular radial RFs. The reason is that the method focuses on removing the effect of random noise, but not coherent noise components. In regular radial RFs, a coherent noise component dominates, which is the structure-generated signal due to reverberations in the shallow sedimentary cover.

Tables S1–S3 provide for the three subarrays the final number of RFs obtained at each station.

3. Synthetic Experiments

We present in Figure 2 the Crust1.0 structure and corresponding synthetic radial and vertical RFs for selected stations ordered by increasing thickness of the sedimentary cover in Crust1.0. Radial RFs have been computed through water-level deconvolution following Equations 4 and 5 (Figure 2b). Vertical RFs are calculated using autocorrelation and spectral whitening following Equations 1 and 2 (Figure 2c). Generally, the vertical RFs provide good predictions for the Moho depth for all selected stations for all the velocity models. However, the radial RFs are more complicated. For a crustal cover without SB (P56A), the "Moho pulse" appears at the true depth and is reliable. For a thin sedimentary cover (QUA2), oscillations due to reverberations are very strong at shallow depth, while the "Moho pulse" can still be distinguished in the radial RF. The converted pulses are followed by short duration and low-amplitude oscillations associated with post-cursory shear-wave reverberations of the converted wave in the thin sedimentary layer. For thicker sedimentary covers, the "Moho pulses" are not reliable anymore. The pulses result from the interference of conversions at the Moho discontinuity and multiple reverberations (Figure 2b, station Sets 3, 4, and 5). The Moho pulse cannot be distinguished from shallow multiples. In addition, the maximum amplitude on the radial RF is not the P-wave peak but the conversion at the base of the basin. This suggests that vertical RFs as processed here will be a more reliable source of information about the deep crustal structure than radial RFs.

4. Results

4.1. Results for the Three Subarrays

We show in Figures S5–S7 examples of vertical RF stacks for three selected transportable array stations from Subarray I. For these stations, and despite a 2-year duration of acquisition, there is no apparent loss in quality of the stacked autocorrelograms with respect to a permanent station such as HRV (Figure S4). The data selection slightly improves the lateral continuity of signals when building a profile from stations

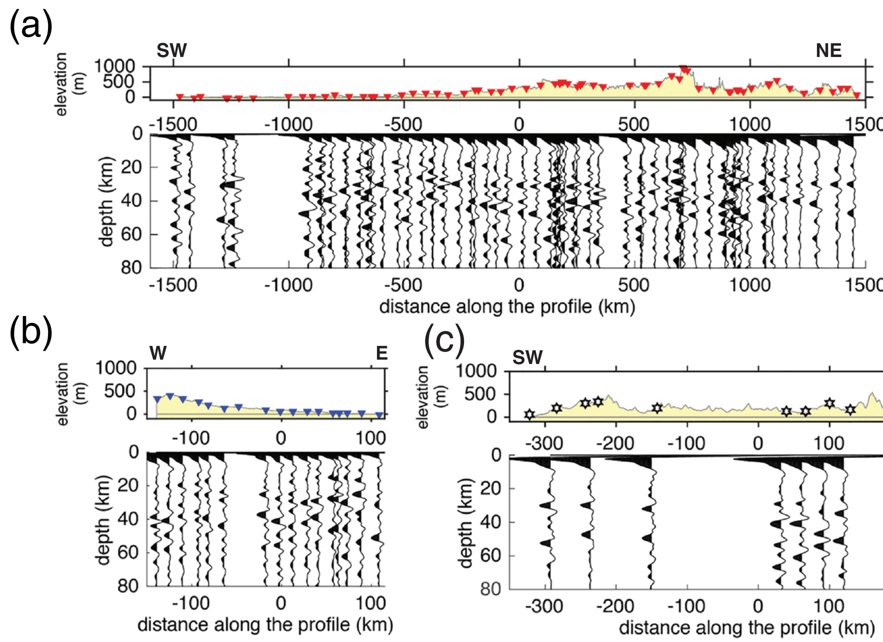

Figure 3. *P*-wave autocorrelation signals (black traces) along the three subarrays in Figure 1c. The arrays are (a) Subarray I, (b) Subarray II, and (c) Subarray III. The top panel in each subplot presents the topographic profile (Smith & Sandwell, 1997), with markers positioning seismic stations. The bottom panels are the observed autocorrelograms (black traces) in the depth domain. To target the Moho, the vertical RFs are processed with $W = 0.1$ Hz and a postprocessing filter with 0.2- to 1.0-Hz band pass.

with variable numbers of earthquake records (Figure S8). For 71 stations in Subarray I, 10 stations have a set of less than 15 RFs, which are discarded, and among the remaining 61 stations, 43 stations have no more than 50 waveforms. The application of bootstrap resampling allows to estimate the variability of stacked waveforms and demonstrates that we observed robust signals (Figure S9).

Overall, the vertical RFs are relatively simple with two, at maximum three, major pulses (Figure 3). This is in contrast with the radial RFs, which show significantly more complexity (see section 5.2; Figure 7). Chains of pulses are consistently observed along the three profiles at ~30 and ~40 km depth (Figure 3), likely associated with the deepest crustal layering. Yet, it can be relatively complicated to interpret vertical RFs in terms of a deterministic structure. Multiple arrivals with similar amplitudes are recovered at crustal levels, making the identification of the Mohorovičić discontinuity ambiguous. In some cases, arrivals are detected at lithospheric mantle depth, for example, at the southwestern portion of Subarray III (Figure 3c), where the Moho is not expected to lie deeper than 35 km according to Crust1.0 (Figure 1e). Although we cannot take the structure provided by Crust1.0 as the ground truth, we can interpret this deep signal as a fictitious interface that results from the arrival of multiple reverberations with cross-mode coupling, *PPs* (see Figures 1a and 1b and synthetic experiment based on Crust1.0 in section 4.2).

A priori geological and seismological information show that major Holocene to Cenozoic SB structures are sampled by Subarrays I and II (Figures 1d and 1f). Yet, we do not observe significant lateral variations of signal quality when the arrays cross such structures (Figure 3a). We will show in section 5.2 that this is a clear advantage of the vertical RFs over the traditional radial RF method.

4.2. Comparison with Crust1.0

We first use Crust1.0 as a reference crustal model for comparison, but not acting as constraint to interpret crustal structures. In a second step, we use Crust1.0 as a guide for identifying and picking the Moho interface on vertical autocorrelations. Autocorrelations are plotted against Crust1.0 *P*-wave velocities in the background of Figure 4. The three SB layers are marked with dark blue colors (sed.), the crustal layers as light blue to brown (upper, middle, and lower crust; u.c., m.c., and l.c.), overlying the mantle (m.) in yellow. This a priori seismological structure allows a more confident interpretation of the horizons detected with vertical autocorrelations. In all three profiles, we observe a rough agreement between the large negative peaks

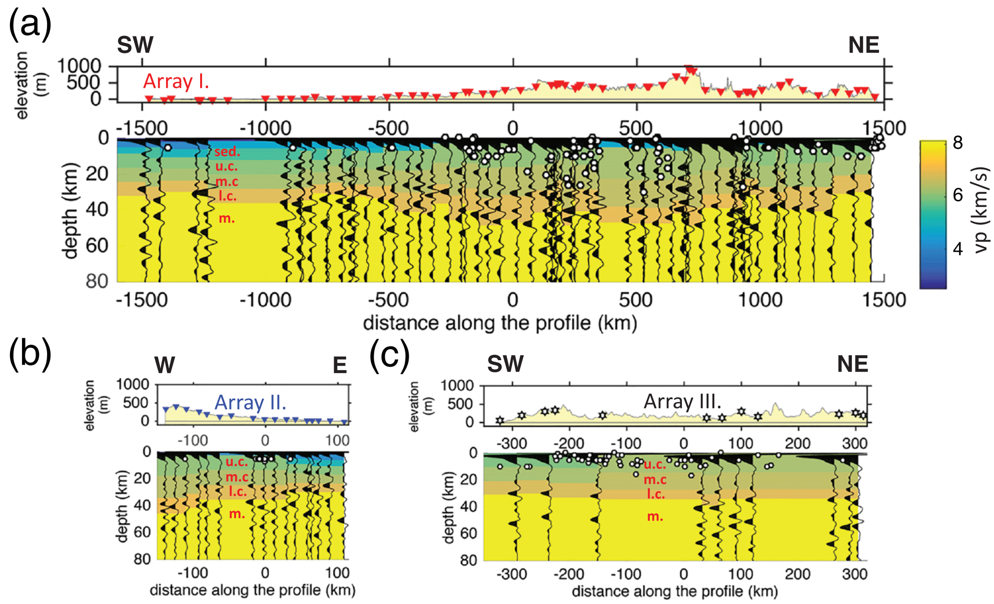

Figure 4. Superimposition of observed *P*-wave autocorrelation signals (black traces) to the *P*-wave velocity structure (background colors) in the reference crustal model Crust1.0 (Laske et al., 2013). The white circles are associated with the local seismicity (USGS catalog; see Figure 1c). The layers are sed. (sedimentary layers), u.c. (upper crust), m.c. (middle crust), l.c.(lower crust), and m. (mantle).

in observed data and the velocity model. There is good but not perfect agreement between the strongest amplitude negative pulses observed on autocorrelations and the base of the crust (brown-to-yellow transition). We find that the northeast portion of Subarrays I and III both produce the best match with the Moho depth in Crust1.0, where the crust contains no sedimentary layers and is the most laterally homogeneous.

We propose in Figure 5a a guided picking of interfaces of the crust, where the purple horizon represents the Moho discontinuity and the shallower blue horizon an intracrustal discontinuity. We demonstrate here that extracting coherent information about *P*-wave reflections from event-based vertical RFs/autocorrelations

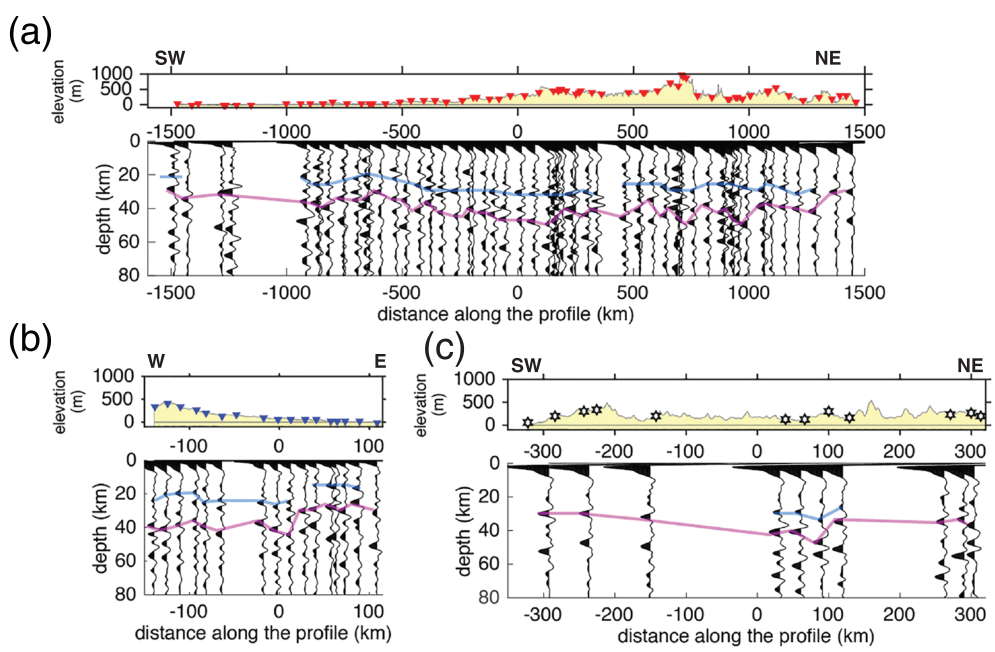

Figure 5. (a–c) The same as Figure 3, but now with the proposed picks of laterally continuous crustal interfaces. The light purple horizon represents the Moho discontinuity and the shallower, blue horizon, an intracrustal discontinuity.

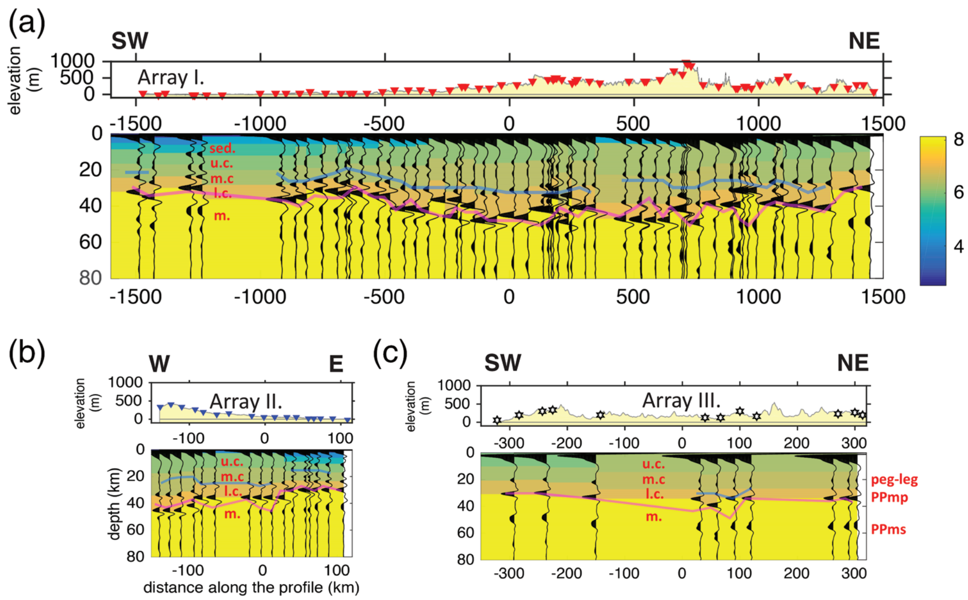

Figure 6. (a–c) Superposition of synthetic *P*-wave autocorrelation signals (black traces) to the *P*-wave velocity structure (background colors) in the global crustal model Crust1.0 (Laske et al., 2013). The light purple and blue horizons are the same as Figure 5.

computed from temporary networks and dense arrays is feasible. The continuous horizon between 20- and 30-km depth on the profile obtained from Subarray I in blue (Figure 5) is consistent with a reflective interface at the top of the lower crust. A number of arrivals at shallower and deeper levels have low-amplitude and/or poorer lateral continuity, so are more difficult to interpret. The comparison between Figures 4 and 5 suggests that transportable array data are of sufficient quality to highlight with autocorrelations the crustal internal stratification.

However, there are differences (Figure 4): (a) there exist minima and maxima in the vertical RFs that are not associated with discontinuities as described by Crust1.0, in particular, in the lithospheric mantle; (b) many small amplitude arrivals might correspond to features present in the Crust1.0 model but are slightly offset; (c) along the 250-km extent of the linear Subarray III, the data reveal variations of Moho topography (Figure 4b) that are not present in the model; (d) at depths <10 km, the response loses its interpretability as it appears dominated by signal-processing artifacts.

For further comparison, we computed the synthetic vertical RFs for the Crust1.0 model with the same acquisition geometry as observed in the data (Figure 6). This synthetic experiment demonstrates that vertical RFs are fairly simple and, in theory, most of the predicted pulses can be deterministically attributed to interfaces in the input model, although some secondary arrivals at crustal depth and in the uppermost mantle can be attributed to "peg-leg reverberations" or cross-mode contamination (PPms). In addition, this synthetic experiment shows that the method, with this choice of parameters ($f_{min} = 0.2$ Hz and $W = 0.1$ Hz), suffers from a loss in resolution at shallow depth (<10 km). This is the result of the pronounced side lobe of the peak at zero lag in the autocorrelations.

We can draw three important conclusions from the comparison of Figures 4 and 6. First, observed vertical autocorrelations are more complex than predicted based on Crust1.0, suggesting that there exist at crustal level small-scale heterogeneities and/or 3D effects of wave propagation that are not captured using the reference model. Second, our method successfully recovers the crustal information without loss of signal-to-noise ratio or increased complexity in regions with thick sedimentary cover. This latter conclusion is supported by both the synthetic and observed data in the southwest portion of Subarray I and eastern portion of Subarray II (Figures 4 and 6). Finally, in the observed data, *P*-wave reflections from the top of the Moho discontinuity are consistently observed with lower amplitudes than predicted by the Crust1.0 model (Figures 4 and 6). In contrast, reflected pulses associated with intracrustal discontinuities have a similar or slightly higher amplitude than predicted by Crust1.0.

Figure S10 shows a negative correlation (−0.58) between our observed crustal thickness and the thickness of the sedimentary cover in the Crust1.0 model. This anticorrelation is predicted for a crust in isostatic equilibrium. The fit of a theoretical model to our best fitting line is obtained for a sediment density of 2.15 g/cm^3, which is within the continental average range of densities for soft (2.07 g/cm^3) and hard (2.38 g/cm^3) sediments in the Crust1.0 model (Laske et al., 2013).

5. Discussion

5.1. On the Interpretation of Autocorrelations

As presented in our results section, we unambiguously identify two chains of pulses near 30- and 40-km depth. From synthetic experiments and using of independent information (Crust1.0 model), we demonstrated that these chains of pulses are related to the reflections from the upper side of the Moho discontinuity, namely, PPmp and PPms, and from the top of the lower crustal layer. Due to the limited number of data and intrinsic characteristics of the Moho boundary (see section 5.4), it can, however, be challenging to unambiguously pick the PPmp phase on autocorrelations. This is not a unique problem to our particular data set, as most other prior studies based on autocorrelations suffer from similar interpretation problems (cross-mode contaminations and narrow frequency band limiting the resolution of velocity gradients) (e.g., Becker & Knapmeyer-Endrun, 2018; Gorbatov et al., 2013; Saygin et al., 2017; Sun & Kennett, 2016; Taylor et al., 2016; Tibuleac & von Seggern, 2012). In addition, we show in the next section that the vertical RFs behave better than radial RFs in the presence of a sedimentary cover. We therefore cast our analysis as a reference for future interpretations based on this technique.

Tauzin et al. (2019) showed that the lateral sampling of the PPp mode increases with the depth of investigation and the difference with typical *Ps* conversion modes used in the radial RF imaging is of the order of 5 km at the depth of the Moho. This means that, in the single-station stacking, the cone of sensitivity of the *P*-wave reflections surrounding the stations will have a 10- to 20-km diameter (this distance is slowness dependent) while it will have only a 5- to 10-km diameter for the *Ps* conversions. As such, station-based gathering will be slightly more vulnerable to the presence of strong lateral variations in the Moho depth (crustal thickness) than in the radial RF imaging.

The effect will be a slight decrease in amplitude of the reflected phase due to out-of-phase stacking. In addition to lateral variations of the Moho, crustal heterogeneity and surface topography both contribute to the PPmp-P differential travel time. The maximum topographic difference in our study is about 1 km. We estimate the delays introduced by a 1-km topography of the Earth surface and at the Moho discontinuity to be 0.8 and 0.3 s, respectively. Such delays are significant, but smaller than the width of the reflected pulse (1 s). Consequently, if topographic variations over the area surrounding the station may contribute to the decrease in amplitude of the PPmp reflected pulse, they are unlikely to explain the whole difference with Crust1.0. This conclusion is also supported by the observation that the PPmp amplitudes are remarkably consistent across all of our images and appear uncorrelated with local gradients in surface topography. An additional strong argument for a negligible effect of surface topography is the observation of the reflections from the top of the lower crust with amplitudes similar as predicted by model Crust1.0. We conclude that the difference between the observed and the Crust1.0 Moho amplitudes must therefore have another origin (see section 5.4).

In Figure S11, we present an image of the crustal structure along the Subarray II based on the CRP stacking method (Tauzin et al., 2019), accounting for the geometry of illumination of the structure by the PPp mode. Subarray II is better positioned for performing such an experiment as the interstation distance is the smallest among the three subarrays considered here. The image remains consistent with the observed structure from the single-station stacking, although the portions of the image with poor ray coverage suffer from a low signal-to-noise ratio.

5.2. Radial Receiver Functions

We present in Figure 7 stacked radial RFs for the three subarrays. Corresponding seismic sections are shown for the observed data and for the predictions from Crust1.0, both superimposed to the v_p structure in Crust1.0. Because each interface generates a triplet of phases (*Ps*, *PPs*, and *PSs*), the crustal structure has less readability than in the case of vertical RFs, even in the synthetic case (compare Figure 7b to Figure 6a).

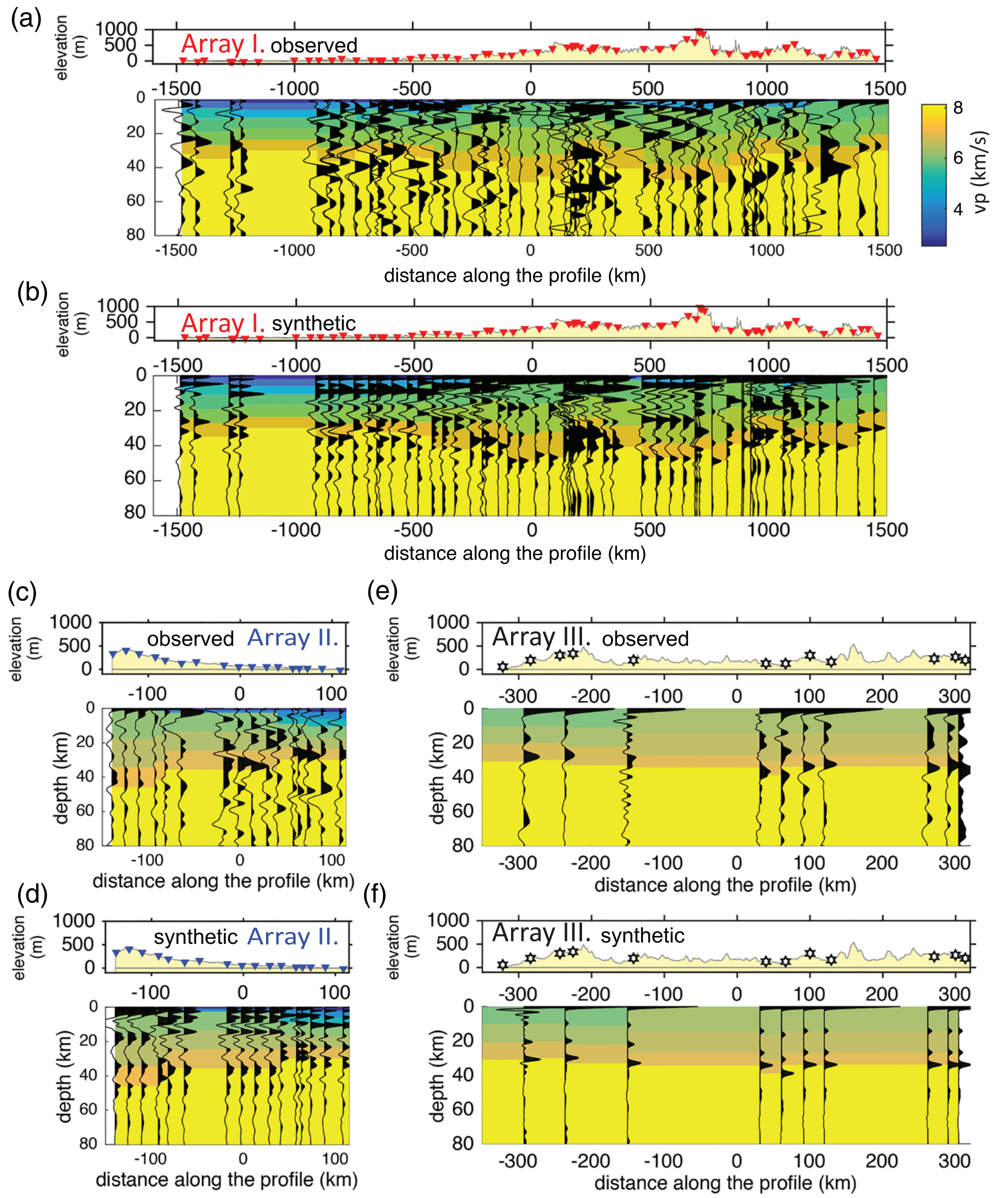

Figure 7. Observed (a, c, and e) and synthetic (b, d, and f) radial receiver functions (black traces) superimposed to the *P*-wave velocity structure (background colors) in the global crustal model Crust1.0 (Laske et al., 2013). The other panels are synthetics. No postprocessing filtering is applied.

The simplest radial RFs are obtained for Subarray III because the crust does not include a near-surface sedimentary cover. In this case, the Moho has the strongest amplitude and the maxima of converted *Ps* pulses can easily be associated with crustal interfaces (Figures 7e and 7f).

When one or several low-velocity sedimentary layers are present, radial RFs get more complicated. Instead of being dominated by positive pulses associated with increases of velocity/impedance at intracrustal discontinuities (Figures 7e and 7f), radial RFs incorporate a strongly oscillating component (Figures 7a–7d) with unreliable converted pulses associated with the Moho discontinuity. This behavior is easily explained by the synthetic experiment shown in section 3. In conclusion, even in the absence of noise of natural origin, the radial RFs are less reliable tools than the vertical RFs when low-velocity sedimentary layers exist near the surface. In comparison, the vertical RFs are simpler to interpret, although it is fair to say that they are not void of artifacts related to these shallow reverberations. We discuss the effect of reverberations and SB structure in section 5.3, together with the impact of playing with the width of the smoothing window

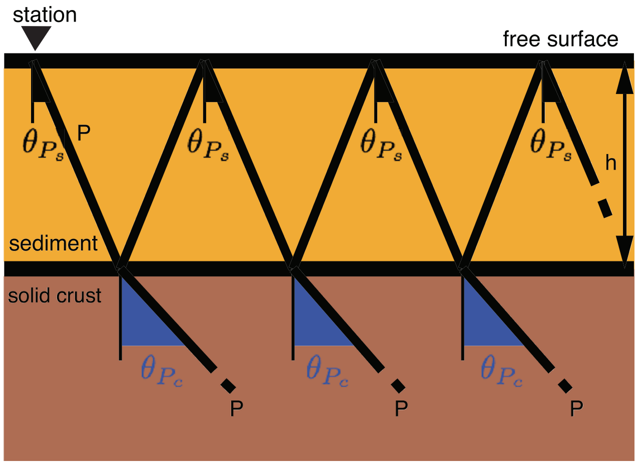

Figure 8. Sequence of reverberations in a sedimentary layer. The seismic station (black inverted triangle) sits on a sedimentary layer (orange) above the solid crust (brown). The direct P wave reaches the discontinuity between the sedimentary layer and the solid crust and generates a first-order P wave. Due to the significant impedance contrast, the first-order P waves reverberate multiple times inside of the sedimentary layer. The thickness of the sedimentary layer is denoted as h. θ_{P_c} and θ_{P_s} are the incident angles of P waves in the crust and sediment layer, respectively.

W for spectral whitening. We show in particular that a well-chosen value of W significantly improves the readability of the crust because spectral whitening can act as a resonance removal filter.

5.3. Filtering Out Basin Resonance Through Spectral Whitening

In SBs, a strong resonance effect is recorded on the vertical component as P-wave reverberates multiple times in the low-velocity sedimentary cover. Figure 8 shows the sequence of P-wave reverberations in a simple sedimentary structure, with a single layer. The sedimentary layer has lower velocities than the half space beneath it. Teleseismic P waves reach the basement of the sedimentary layer and transmits as first-order P waves. The reflection of P waves at the free surface is almost a total reflection. Due to the significant impedance contrast at the base of the sedimentary layer, the free-surface reflected P waves reverberate multiple times inside the sedimentary layer. These reverberations contribute to a strong resonance effect, which is recorded by the receiver on the Earth's surface mainly on the vertical component. In the time domain, these reverberations correspond to strong amplitude pulses that contaminate the seismograms. A remark is that on the vertical component, interference effects from converted S waves are small because of the extremely low-incidence angle of P waves due to the slow velocities in the SB layer.

To understand the reverberations caused by SBs, we use an example with a sedimentary layer over a half-space bedrock. The power spectrum of an impulse wavefront at normal incidence through a sedimentary layer over a half-space bedrock can be expressed as

$$|Z(f)| = \frac{1-r}{1+r} \cdot \frac{1}{(1+(re^{-2\pi f Q})^2 - 2re^{-2\pi f Q}\cos 2\pi f \tau)^{\frac{1}{2}}}. \tag{7}$$

where details can be referred to Appendix A in Pham and Tkalčić (2018) for the full derivation of Equation 7 using the matrix propagation method (Claerbout, 1968; Kennett, 1983). In Equation 7, $r = (\rho_s v_s - \rho_c v_c)/(\rho_s v_s + \rho_c v_c)$ is the reflection coefficient at the SB-crust interface in a downward direction. ρ and v are the density and wave speed of the media, where subscript $_s$ refers to the SB and $_c$ to the crustal rock. $\tau = 2h/v$ is the two-way travel time in the layer. Q is the attenuation factor of in the sediment layer.

The spectral response in Equation 7 is a function in the frequency domain, which is characterized by peaks that are equally spaced at resonance frequencies,

$$f_n = \left(n + \frac{1}{2}\right) \cdot \frac{1}{\tau}. \tag{8}$$

Despite the fact that Equation 7 is derived for normal incidence, it represents a good approximation for slight oblique incidence (see Figure S12). This shows that the contribution of converted S wave on the vertical component in slightly oblique incidence is negligible.

In Equation 2, the frequency-dependent spectral-whitening operation allows balancing the frequency content of the RFs (Bensen et al., 2007; Pham & Tkalčić, 2017; Tauzin et al., 2019), and also removing specific spectrum-maxima related to the resonance of the layered structure beneath a receiver. To illustrate this, we proceed with a numerical experiment with simple one-dimensional models (Figure 9). The first model has a one-layer crust (no SB). The second model has a two-layer crust including a layer near the surface with low velocities mimicking the effect of a sedimentary cover (SB model). This layer is 2-km thick. The Moho is located at 30-km depth in both models. The elastic parameters chosen for the SB layer and the contrast in impedance across its base are consistent with the structure given for station QUA2 in Crust1.0.

We simulate vertical-component waveforms with the same plane-wave matrix algorithm (Kennett, 1983; Randall, 1989). Figure 9b shows the results of the numerical experiment in the time-domain for vertical component waveforms. In addition to the peak at zero lag, the black trace (no SB model) shows the pulses of the P-wave reflection at the Moho (PPmp). For the SB model (red trace), the large contrast of elastic

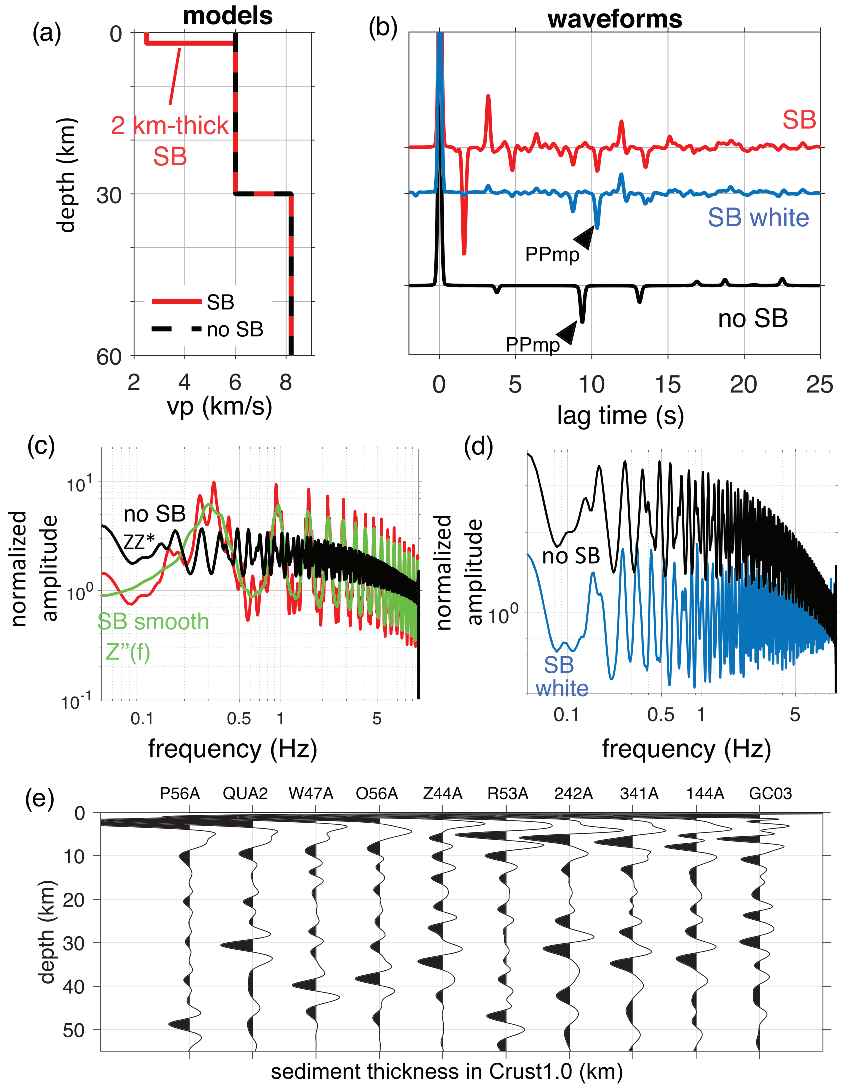

Figure 9. Numerical experiment illustrating turning off the resonance associated with a shallow sedimentary layer. (a) Crustal velocity models with a "normal" crust (no SB) and a sedimentary basin (SB model). (b) Simulated vertical responses aligned by *P*-wave arrival. The black seismogram is the vertical response for the normal crust (no SB). The red one is for the sedimentary basin (SB model). The blue one is the result of spectral whitening for the SB model (SB white). Major identified phases are the *P*-wave reflections (PPmp) and the *P*-to-*S* reflection (PPms) above the Moho. The slowness is $p = 0.06$ s/km. (c) Spectra $Z(f)$ of the vertical component responses. The spectra in black and red represent the responses ZZ^* for the normal crust (no SB) and sedimentary basin (SB model), respectively. The spectrum in green represents the smoothed response $Z''(f)$ for the SB model. (d) The spectrum after spectral whitening for the SB model (blue), compared with the spectrum for the "normal crust" model (black). (e) Synthetic vertical autocorrelations for the same 10 stations as in Figure 2 computed with $W = 0.4$ Hz. Combined with Figure 2c, this figure shows filtering on or off the resonance in the shallow sedimentary cover with different values of smoothing parameter W.

properties at the base of the SB introduces a strong resonance effect which contaminates the seismic response. This resonance corresponds to the ringing due to *P*-wave reverberations in the shallow sedimentary layer (Equation 7). This makes it difficult to distinguish the reflection at the base of the crust (Figure 9b). In the frequency domain (Figure 9c), the fundamental-mode resonance on the red spectrum appears as a broad and strong amplitude peak centered at ∼0.3 Hz, consistent with the 2-km thick, near-surface layer according to Equation 3.

Spectral whitening offers a way to turn off such a resonance. The first step consists in smoothing the vertical component spectrum running an average over the predefined width W. We use $W = 0.1$ Hz in this example (Figure 9c). The smoothed spectrum (green) only preserves the broad peaks due to resonance in the shallow sedimentary layer. The deconvolution in the frequency domain (Equation 1) gives a spectrum close to the model without SB (Figure 9d), and the exponentially decaying ringing is partially removed from the corresponding time-domain trace (Figure 9b). The whitened SB trace can now be interpreted, in particular to find the phase reflected at the Moho discontinuity. A residual ringing persists because the spectral whitening does not completely filter out the effect of the shallow SB on the vertical component spectrum.

Figures 9e and 2c compare synthetic vertical autocorrelations for the various structures shown in Figure 2a and show the effect of choosing different values of W. Choosing a large value of W (here $W = 0.4$ Hz) corresponds to applying the autocorrelation method without turning on the resonance removal filter (Figure 9e). When using $W = 0.1$ Hz, oscillations associated with SB reverberations are damped, and this eases the interpretation of the crustal structure (Figure 2c). In general, $W = 0.1$ Hz is a reasonable value to choose when targeting a Moho near 35-km depth.

Initially designed for improving the resolution of autocorrelations (Pham & Tkalčić, 2017), spectral whitening is a simple method that also acts as a resonance removal filter. Here, we demonstrate that spectral whitening can effectively remove the resonance associated with SB. There exist other methods performing such a function. For example, Yu et al. (2015) used RFs to determine the crustal structures for seismic stations on top of a low-velocity sedimentary layer. They applied autocorrelation with a resonance removal filter in the frequency domain to reduce the amplitude of reverberations in the layer. Langston (2011) used downward continuation and wave-field decomposition to reduce the effect of SB reverberations. This method requires a prior knowledge of the Earth structure and modeling to extract *Ps* conversions from the deeper crust. Tao et al. (2014) used wavefield downward continuation to estimate sedimentary and crustal structure. The same authors used the H-κ grid-searching technique to study the Moho depth and average v_p/v_s ratio. They applied H-β method to remove the reverberations caused by unconsolidated sediments. Yang and Niu (2019) studied sedimentary structure of basins in China from frequency-dependent *P*-wave particle motion. Li et al. (2019) successfully isolated the Moho *P*-to-*S* conversion from sediment reverberations with a wavefield-downward-continuation technique. They reported a joint inversion that can retrieve the input sedimentary models. A comprehensive comparison between these methods and the resonance removal filter described here would be interesting but is out of the scope of this study.

5.4. The Moho as a Transitional Layer

In high-frequency (>10 Hz) active seismic reflection experiments, it is common to observe a laterally variable crustal reflectivity between geological terraces, but also a vertical contrast in reflectivity at the transition between the crust and upper mantle (e.g., Kennett & Saygin, 2015). The Mohorovičić discontinuity is regularly identified as the base of the lower crust, but is often itself not marked by a strong reflectivity. The upper mantle shows no distinct reflections probably because the vertical scale of the structure is longer than the seismic wavelength used in active reflection surveys (Kennett & Furumura, 2016). At the same time, seismic surveys based on radial RFs with lower frequency content (<1 Hz) point at the Moho being the most reflective interface.

The Moho is a first-order discontinuity in Crust1.0 with contrasts of ~16% in v_p and ~13% in v_s and density. Here, we find that amplitudes of low-frequency (0.2–1.0 Hz) *P*-wave reflections on top of the Moho, measured using autocorrelations (Figure 4), are weaker than predicted by the Crust1.0 model (Figure 6). We discussed in section 5.1 the effects of surface and boundary topography, pointing that these are unlikely explanations for such weak amplitudes. We here consider three alternative scenarios: (a) the elastic impedance contrast at the boundary is smaller than predicted by Crust1.0, (b) there is an effect of anelasticity that is not accounted for in the seismic modeling, and/or (c) the Moho is a transitional layer rather than a sharp boundary. The first scenario is unlikely as a smaller impedance contrast would lead to decreased *Ps* conversion amplitudes on radial component RFs as well. Nonetheless, where observed, the pulse of the direct Moho *Ps* (Figures 7a, 7c, and 7e) conversion has a similar amplitude as predicted by Crust1.0 (Figures 7b, 7d, and 7f). For the same reason, the second case is unlikely. The effect of attenuation is expected to be stronger on shear waves than on *P* waves, thus should affect more responses on the radial components.

For petrological reasons, the seismic Moho is likely a gradual transition (e.g., Arndt & Goldstein, 1989; Dufek & Bergantz, 2005; Furlong & Fountain, 1986; Thybo & Artemieva, 2013; White & McKenzie, 1989). We demonstrate here that a gradual transition could jointly explain our observations of amplitudes for topside

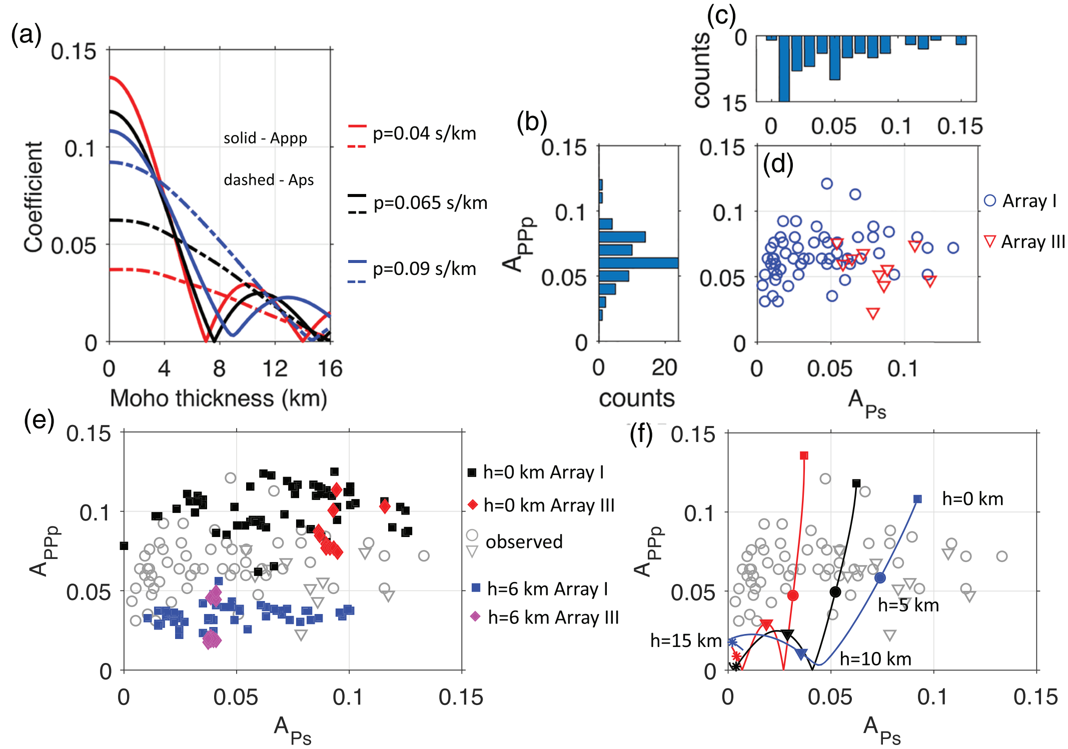

Figure 10. Sensitivity of PPmp reflections and Pms transmissions to a gradual Moho layer. (a) Variation of the topside *P*-wave reflection coefficient *Rpp* (solid lines) and bottom-up transmission coefficient Tps (dashed lines) with the thickness of the velocity gradient at the Moho. Coefficients are calculated for a *P* plane wave with different slowness: $p = 0.04$ s/km (red), $p = 0.065$ s/km (black), and $p = 0.09$ s/km (blue). Here, the elastic properties across the Moho are defined by Crust1.0 for station KVTX in Subarray I. The value of coefficient is taken in the middle of the frequency band used in an analysis of vertical RFs (0.2 −1.0 Hz). (b) Histogram of measured amplitude of reflections (A_{PPp}) for Subarrays I and III. (c) Histogram of measured amplitude of conversions (A_{Ps}) for Subarrays I and III. (d) Measured amplitudes of reflections (A_{PPp}) as a function of amplitudes of transmissions (A_{Ps}) for observed data of Subarrays I (blue circles) and III (red triangles). (e) A_{PPp} versus A_{Ps} from synthetic data with Moho thickness h = 0 km and h = 6 km (rectangle and diamond points) and observed data (gray circles and triangles). Data belongs to Subarrays I and III. (f) Theoretical curves of A_{PPp} as a function of A_{Ps}, with points indicating the Moho thickness ($h = 0$, 5, 10, 15 km). The gray points are extracted from observed data that is same as Panel (c).

P-wave reflections from vertical autocorrelations and *P*-to-*S* transmissions on radial RFs. *P*-wave reflections and *P*-to-*S* transmissions have a different sensitivity to velocity gradients (e.g., Bostock, 1999; Tauzin et al., 2019). We illustrate this by plotting the transmission and reflection coefficients *Tps* and *Rpp* as a function of the vertical extent *h* of a transitional layer adopting the contrasts in elastic properties for the Moho from Crust1.0 (Figure 10a). For this computation, we decompose the gradient in thin homogeneous layers and use a plane-wave matrix algorithm (Chapman, 2003; Ma et al., 2012; Tauzin et al., 2019). We use a reference frequency of 0.6 Hz, which is the center of the frequency band of analysis for long-period vertical RFs. We also show the coefficient dependence on various slowness. Generally, the transmission coefficients *Tps* decrease smoothly from a sharp interface to an ~10-km-thick interface. In contrast, the reflection coefficients *Rpp* decrease abruptly and nonlinearly with *h* from ~10% to 0% and reach at 0.6 Hz a minimum for an ~8-km-thick layer. This means that a transitional layer tends to affect the reflectivity of *P*-wave reflections more than the reflectivity from direct *P*-to-*S* conversions (Bostock, 1999; Tauzin et al., 2019).

When possible, we measured the amplitudes of the Moho conversions and reflections on the stacked observed vertical and radial waveforms for Subarrays I and III from Figures 3 and 7. Those observations are shown in Figures 10b–10d, 10e (gray), and 10f (gray). As shown by observation histograms in Figure 10b–10c, the distribution of amplitude of the Moho reflection A_{PPp} has a maximum at 6%, whereas the amplitudes of conversion are more uniformly distributed over the range 0%–15%. We observe a larger scatter in A_{Ps} than in A_{PPp}. These observations can be explained by the following: (a) the larger scatter in A_{Ps} can result from the effect of slowness variations, which is stronger on *P*-to-*S* conversions than on *P*-*P* reflections (Figure 10a);

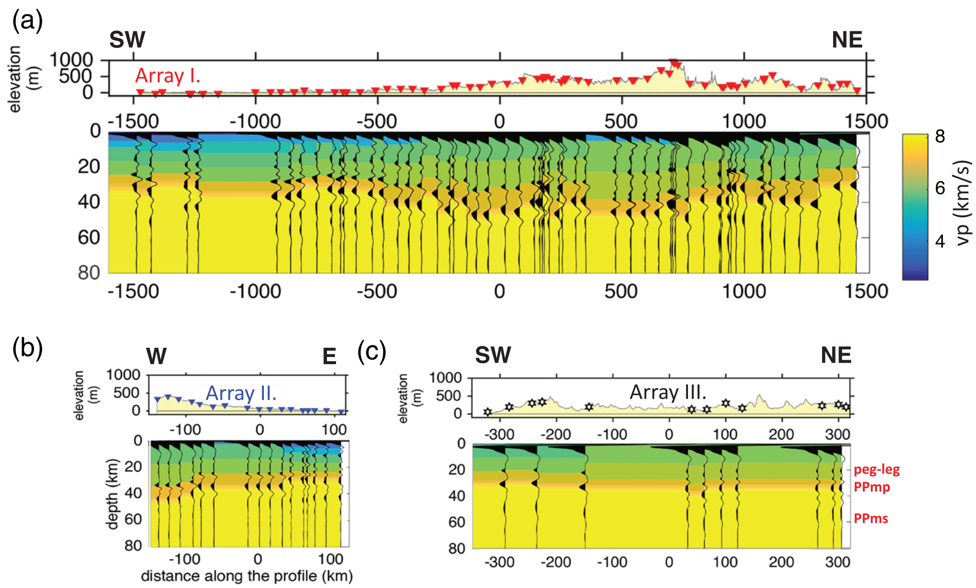

Figure 11. Superposition of synthetic *P*-wave autocorrelation signals (black traces) to the *P*-wave velocity structure (background colors) in the global crustal model Crust1.0 (Laske et al., 2013) modified using a transitional Moho layer 6-km thick.

(b) the A_{Ps} scatters more in Subarray I (with SBs) than Subarray III (on a simple crust), possibly due to the effect of interferences from reverberations in shallow SB layers. Those effects can be simulated through wave propagation in the Crust1.0 structure (Figures 10e, 6, and 12). The synthetic experiments confirm larger scatter in A_{Ps} for Subarray I, which spreads between ~0% to more than 10%, while the coefficients A_{PPp} fall within the ranges of 8%–12% for a Moho width $h = 0$ km (black squares) and 2%–6% for $h = 6$ km (blue squares). Meanwhile, results from Subarray III (red and magenta diamond points) have narrow distributions in A_{PPp} and A_{Ps}, possibly due to the exemption of contaminations by shallow SB layers. In conclusion, A_{PPp} offers more reliable constraints on the values of h. Therefore, from Figure 10f, we find that the solution explaining the amplitudes of the reflections is a transitional layer with a thickness slightly smaller than 5 km. In Figure 11, we show the predicted waveforms for a 6-km-thick gradient, from which we reported the measurements shown in Figure 10d. The predicted Moho amplitudes appear to be in better agreement with the observed data (Figure 4) than the predictions from a first-order discontinuity (Figure 6). We note that the Moho transition can also be reduced to a value thinner than 5 km if we consider a combination of possible mechanisms that can reduce the Moho reflection amplitudes, such as crustal transmission losses, 3D scattering, and effects of inelastic attenuation. However, we would have to explain why such mechanisms do not affect similarly the reflections from the top of the lower crust.

6. Conclusion

We investigated the efficiency of an autocorrelation technique to extract vertical component receiver functions from teleseismic earthquake data and create images of the crust beneath dense seismic arrays. Using synthetic and field-data examples, we compared the performances of both vertical and radial RFs. We examined in particular the contribution of reverberations in shallow sedimentary (SB) layers to the images formed from both data types. Vertical RFs are simpler to interpret than radial RFs, although they are not void of complexities associated with shallow reverberations. We show that the operation of spectral whitening is critical for obtaining good quality images beneath SBs, as it acts as a resonance removal filter. We processed broadband data from three temporary US subarrays with quasi-linear geometry in the eastern United States. By identifying pulses of reflected *P* waves on the vertical autocorrelograms, we were able to identify the Moho and a laterally variable crust structure beneath these subarrays. We observed coherent signals along the three subarrays despite the presence of SBs. Compared with the crustal model Crust1.0, our analysis suggests the existence of additional complexity related to fine-scale layering and/or 3D structure. We developed a method to constrain the thickness of the Moho boundary from an amplitude analysis of reflected and converted phases on vertical and radial component RFs. This analysis shows that the Moho beneath eastern

United States is a transitional layer extending over a depth interval of up to 5 km. The proposed method is highly complementary to other receiver-based methods and has the potential to advance our understanding of the crustal architecture with or without SBs.

Data Availability Statement

The IRIS Data Management Center was used for access to waveform data (available from http://service.iris.edu/fdsnws/dataselect/1/).

Acknowledgments
The facilities of IRIS Data Services, and specifically the IRIS Data Management Center, were used for access to waveforms, related metadata, and/or derived products used in this study. IRIS Data Services are funded through the Seismological Facilities for the Advancement of Geoscience and EarthScope (SAGE) Proposal of the National Science Foundation under Cooperative Agreement EAR-1851048. Data from the TA network were made freely available as part of the EarthScope USArray facility, operated by Incorporated Research Institutions for Seismology (IRIS) and supported by the National Science Foundation, under Cooperative Agreements EAR-1261681. Access to the Crust1.0 model were obtained at https://igppweb.ucsd.edu/~gabi/crust1.html. We acknowledge the very constructive comments from reviewer Elmer Ruigrok, associate editor Sebastien Chevrot, and an anonymous reviewer. B. T. has received funding from the European Union's Horizon 2020 research and innovation program under the Marie Sklodowska-Curie grant agreement No. 793824.

References

Ahern, T., Casey, R., Barnes, D., Benson, R., & Knight, T. (2007). Seed standard for the exchange of earthquake data reference manual format version 2.4. Incorporated Research Institutions for Seismology (IRIS), Seattle.

Ammon, C. (1991). The isolation of receiver effects from teleseismic P waveforms. *Bulletin of the Seismological Society of America*, *81*, 2504–2510.

Arndt, N. T., & Goldstein, S. L. (1989). An open boundary between lower continental crust and mantle: Its role in crust formation and crustal recycling. *Tectonophysics*, *161*(3–4), 201–212.

Becker, G., & Knapmeyer-Endrun, B. (2018). Crustal thickness across the Trans-European Suture Zone from ambient noise autocorrelations. *Geophysical Journal International*, *212*(2), 1237–1254.

Bensen, G., Ritzwoller, M., Barmin, M., Levshin, A., Lin, F., Moschetti, M., & Yang, Y. (2007). Processing seismic ambient noise data to obtain reliable broad-band surface wave dispersion measurements. *Geophysical Journal International*, *169*(3), 1239–1260.

Bostock, M. (1999). Seismic waves converted from velocity gradient anomalies in the Earth's upper mantle. *Geophysical Journal International*, *138*, 747–756.

Buffoni, C., Schimmel, M., Sabbione, N. C., Rosa, M. L., & Connon, G. (2019). Crustal structure beneath Tierra del Fuego, Argentina, inferred from seismic *P*-wave receiver functions and ambient noise autocorrelations. *Tectonophysics*, *751*, 41–53.

Burdick, L. J., & Helmberger, D. V. (1974). Time functions appropriate for deep earthquakes. *Bulletin of the Seismological Society of America*, *64*(5), 1419–1427.

Burdick, L. J., & Langston, C. A. (1977). Modeling crustal structure through the use of converted phases in teleseismic body-wave forms. *Bulletin of the Seismological Society of America*, *67*(3), 677–691.

Chapman, C. (2003). Yet another elastic plane-wave, layer-matrix algorithm. *Geophysical Journal International*, *154*(1), 212–223.

Claerbout, J. F. (1968). Synthesis of a layered medium from its acoustic transmission response. *Geophysics*, *33*(2), 264–269.

Clayton, R. W., & Wiggins, R. A. (1976). Source shape estimation and deconvolution of teleseismic bodywaves. *Geophysical Journal International*, *47*(1), 151–177.

Delph, J. R., Levander, A., & Niu, F. (2019). Constraining crustal properties using receiver functions and the autocorrelation of earthquake-generated body waves. *Journal of Geophysical Research: Solid Earth*, *124*, 8981–8997. https://doi.org/10.1029/2019JB017929

Dufek, J., & Bergantz, G. (2005). Lower crustal magma genesis and preservation: A stochastic framework for the evaluation of basalt–crust interaction. *Journal of Petrology*, *46*(11), 2167–2195.

Efron, B., & Tibshirani, R. (1991). Statistical data analysis in the computer age. *Science*, *253*, 390–395.

Ekström, G., Nettles, M., & Dziewoński, A. (2012). The global CMT project 2004–2010: Centroid-moment tensors for 13,017 earthquakes. *Physics of the Earth and Planetary Interiors*, *200*, 1–9.

Frederiksen, A., & Delaney, C. (2015). Deriving crustal properties from the *P* coda without deconvolution: The southwestern Superior Province, North America. *Geophysical Journal International*, *201*(3), 1491–1506.

Furlong, K. P., & Fountain, D. M. (1986). Continental crustal underplating: Thermal considerations and seismic-petrologic consequences. *Journal of Geophysical Research*, *91*(B8), 8285–8294.

Gorbatov, A., Saygin, E., & Kennett, B. (2013). Crustal properties from seismic station autocorrelograms. *Geophysical Journal International*, *192*(2), 861–870.

Helffrich, G. (2019). Comment on "Crustal thickness across the Trans-European Suture Zone from ambient noise autocorrelations" by G. Becker and B. Knapmeyer-Endrun. *Geophysical Journal International*, *217*(2), 906–908. https://doi.org/10.1093/gji/ggz072

Kennett, B. (1983). *Seismic Wave Propagation in Stratified Media*. Cambridge, New York: Cambridge University Press.

Kennett, B. (2015). Lithosphere–asthenosphere *P*-wave reflectivity across Australia. *Earth and Planetary Science Letters*, *431*, 225–235.

Kennett, B., & Engdahl, E. (1991). Travel times for global earthquake location and phase identification. *Geophysical Journal International*, *105*, 429–465.

Kennett, B., & Furumura, T. (2016). Multiscale seismic heterogeneity in the continental lithosphere. *Geochemistry, Geophysics, Geosystems*, *17*, 791–809. https://doi.org/10.1002/2015GC006200

Kennett, B., & Saygin, E. (2015). The nature of the Moho in Australia from reflection profiling: A review. *GeoResJ*, *5*, 74–91.

Kennett, B., Saygin, E., & Salmon, M. (2015). Stacking autocorrelograms to map Moho depth with high spatial resolution in southeastern Australia. *Geophysical Research Letters*, *42*, 7490–7497. https://doi.org/10.1002/2015GL065345

King, P. B., & Beikman, H. M. (1974). Geologic map of the United States. USGS Map Distribution.

Langston, C. A. (1979). Structure under mont Rainier, Washington, inferred from teleseismic body waves. *Journal of Geophysical Research*, *84*, 4749–4762.

Langston, C. A. (2011). Wave-field continuation and decomposition for passive seismic imaging under deep unconsolidated sediments. *Bulletin of the Seismological Society of America*, *101*(5), 2176–2190.

Langston, C., & Hammer, J. (2001). The vertical component *P*-wave receiver function. *Bulletin of the Seismological Society of America*, *91*(6), 1805–1819.

Laske, G., Masters, G., Ma, Z., & Pasyanos, M. (2013). Update on CRUST1. 0-A 1-degree global model of Earth's crust. *Geophysical Research Abstracts*, *15*, 2658.

Li, X. Q., & Nábělek, J. L. (1999). Deconvolution of teleseismic body waves for enhancing structure beneath a seismometer array. *Bulletin of the Seismological Society of America*, *89*(1), 190–201.

Li, Niu, Yang, Y., & Tao, K. (2019). Joint inversion of Rayleigh wave phase velocity, particle motion, and teleseismic body wave data for sedimentary structures. *Geophysical Research Letters*, *46*, 6469–6478. https://doi.org/10.1029/2019GL082746

Ma, Y., Wang, R., & Zhou, H. (2012). A note on the equivalence of three major propagator algorithms for computational stability and efficiency. *Earthquake Science*, *25*(1), 55–64.

Pham, T. S., & Tkalčić, H. (2017). On the feasibility and use of teleseismic *P* wave coda autocorrelation for mapping shallow seismic discontinuities. *Journal of Geophysical Research: Solid Earth*, *122*, 3776–3791. https://doi.org/10.1002/2017JB013975

Pham, T. S., & Tkalčić, H. (2018). Antarctic ice properties revealed from teleseismic *P*-wave coda autocorrelation. *Journal of Geophysical Research: Solid Earth*, *123*, 7896–7912. https://doi.org/10.1029/2018JB016115

Piana Agostinetti, N., Martini, F., & Mongan, J. (2018). Sedimentary basin investigation using receiver function: An East African rift case study. *Geophysical Journal International*, *215*(3), 2105–2113.

Randall, G. (1989). Efficient calculation of differential seismograms for lithospheric receiver functions. *Geophysical Journal International*, *99*(3), 469–481.

Romero, P., & Schimmel, M. (2018). Mapping the basement of the Ebro Basin in Spain with seismic ambient noise autocorrelations. *Journal of Geophysical Research: Solid Earth*, *123*, 5052–5067. https://doi.org/10.1029/2018JB015498

Ruigrok, E., & Wapenaar, K. (2012). Global-phase seismic interferometry unveils *P*-wave reflectivity below the Himalayas and Tibet. *Geophysical Research Letters*, *39*, L11303. https://doi.org/10.1029/2012GL051672

Saygin, E., Cummins, P. R., & Lumley, D. (2017). Retrieval of the *P* wave reflectivity response from autocorrelation of seismic noise: Jakarta Basin, Indonesia. *Geophysical Research Letters*, *44*, 792–799. https://doi.org/10.1002/2016GL071363

Schimmel, M., & Paulssen, H. (1997). Noise reduction and detection of weak, coherent signals through phase-weighted stacks. *Geophysical Journal International*, *130*(2), 497–505.

Schruben, P. G., Arndt, R. E., & Bawiec, W. J. (1998). Geology of the conterminous United States at 1:2,500,000 scale a digital representation of the 1974 PB King and HM Beikman map (No. 11). The Survey; For sale by USGS Map Distribution.

Schruben, P. G. A., Bawiec, R. E., King, W. J., Beikman, P. B., & Helen, M. (1994). Geology of the conterminous United States at 1:2,500,000 scale–A digital representation of the 1974 PB King and HM Beikman Map.

Smith, W. H., & Sandwell, D. T. (1997). Global sea floor topography from satellite altimetry and ship depth soundings. *Science*, *277*(5334), 1956–1962.

Sun, W., & Kennett, B. (2016). Receiver structure from teleseisms: Autocorrelation and cross correlation. *Geophysical Research Letters*, *43*, 6234–6242. https://doi.org/10.1002/2016GL069564

Tao, K., Liu, T., Ning, J., & Niu, F. (2014). Estimating sedimentary and crustal structure using wavefield continuation: Theory, techniques and applications. *Geophysical Journal International*, *197*(1), 443–457.

Tauzin, B., Pham, T. S., & Tkalčić, H. (2019). Receiver functions from seismic interferometry: A practical guide. *Geophysical Journal International*, *217*, 1–24.

Taylor, G., Rost, S., & Houseman, G. (2016). Crustal imaging across the North Anatolian Fault Zone from the autocorrelation of ambient seismic noise. *Geophysical Research Letters*, *43*, 2502–2509. https://doi.org/10.1002/2016GL067715

Thybo, H., & Artemieva, I. M. (2013). Moho and magmatic underplating in continental lithosphere. *Tectonophysics*, *609*, 605–619.

Tibuleac, I. M., & von Seggern, D. (2012). Crust-mantle boundary reflectors in Nevada from ambient seismic noise autocorrelations. *Geophysical Journal International*, *189*(1), 493–500.

van IJsseldijk, J., Ruigrok, E., Verdel, A., & Weemstra, C. (2019). Shallow crustal imaging using distant, high-magnitude earthquakes. *Geophysical Journal International*, *219*(2), 1082–1091. https://doi.org/10.1093/gji/ggz343

Vinnik, L. (1977). Detection of waves converted from *P* to *SV* in the mantle. *Physics of the Earth and Planetary Interiors*, *15*, 39–45.

Wapenaar, K., Draganov, D., Snieder, R., Campman, X., & Verdel, A. (2010). Tutorial on seismic interferometry: Part 1—Basic principles and applications. *Geophysics*, *75*(5), 75A195–75A209.

White, R., & McKenzie, D. (1989). Magmatism at rift zones: The generation of volcanic continental margins and flood basalts. *Journal of Geophysical Research*, *94*(B6), 7685–7729.

Yang, C., & Niu, F. (2019). Sedimentary structure of the western Bohai Bay basin and other basins in North China revealed by frequency dependent *P*-wave particle motion. *Geodesy and Geodynamics*, *10*(5), 372–381.

Yu, Y., Song, J., Liu, K. H., & Gao, S. S. (2015). Determining crustal structure beneath seismic stations overlying a low-velocity sedimentary layer using receiver functions. *Journal of Geophysical Research: Solid Earth*, *120*, 3208–3218. https://doi.org/10.1002/2014JB011610

Zheng, T., Zhao, L., & Chen, L. (2005). A detailed receiver function image of the sedimentary structure in the Bohai Bay Basin. *Physics of the Earth and Planetary Interiors*, *152*(3), 129–143.